Anomalous contrast in broadband THz near-field imaging of gold microstructures

ANGELA PIZZUTO,[1,*] XINZHONG CHEN,[2] HAI HU,[3] QING DAI,[3] MENGKUN LIU,[2] AND DANIEL M. MITTLEMAN[4]

[1]*Department of Physics, Brown University, Providence, RI 02912, USA*
[2]*Department of Physics and Astronomy, Stony Brook University, Stony Brook, NY 11794, USA*
[3]*Division of Nanophotonics, CAS Key Laboratory of Standardization and Measurement for Nanotechnology, CAS Center for Excellence in Nanoscience, National Center for Nanoscience and Technology, Beijing 100190, China*
[4]*School of Engineering, Brown University, Providence, RI 02912, USA*
[*]*angela_pizzuto@brown.edu*

Abstract: THz scattering-type scanning near-field microscopy (s-SNOM) has become a powerful technique for measuring carrier dynamics in nanoscale materials and structures. Changes in a material's local THz reflection or transmission can be correlated to changes in electrical conductivity. Here, we perform tip-based THz nano-imaging of subwavelength gold nanostructures and demonstrate image contrast unrelated to any spatially varying material properties. We show that the specific physical configuration of the gold structures can have a strong influence on local excitations which can obscure the sample's true dielectric response, even in cases where the relevant structures are far outside of the spatial region probed by the AFM tip.

1. Introduction

In recent decades, scattering-type scanning near-field optical microscopy (s-SNOM) has become an extremely robust technique for imaging and spectroscopy at the nanoscale [1–3]. Whereas conventional far-field microscopy is limited by diffraction and therefore cannot resolve objects much smaller than the imaging radiation wavelength, s-SNOM has been shown to bypass this limit by several orders of magnitude [4]; a sharp, conical, conductive probe tip is held nanometers above the sample surface, spatially confining light of any wavelength near its apex and permitting imaging with a spatial resolution on the order of the tip radius, which can be far smaller than the incident wavelength. A lock-in detector is referenced to the frequency of sinusoidal tip tapping, and demodulating of higher harmonics can allow for highly effective background suppression and improved imaging resolution [5]. This approach to subwavelength spectroscopy has proven to be effective in the microwave [6,7], terahertz [8–10], infrared [11,12], and visible [13] regions of the spectrum, with important applications in biosciences [14,15], materials physics [16–19], and interfacial chemistry [20,21].

Tip-based imaging is particularly useful in the long-wavelength regime where diffraction otherwise severely limits spatial resolution and characterizing even micron-sized objects is challenging. THz nano-imaging and nano-spectroscopy in particular have been shown to be powerful tools for characterizing the electro-optic properties of a variety of substances, including bulk semiconductors [22], nanostructures [23, 24], topological insulators [25,26], and a variety of 2D materials [19,22,27,28]. Specifically, many studies have successfully demonstrated THz near-field contrast in samples with changing carrier concentration or arbitrarily complex metallization patterns [8,29,30] as evidence of a spatially varying dielectric response. These efforts are facilitated by electrostatic models which have been developed to describe the complex tip-sample interaction [31–33].

However, changes in the amplitude of scattered near-field radiation may result from factors other than changes in the local dielectric properties of the material underneath the tip, and as these models become more accurate and THz near-field detection methods improve, it will be absolutely necessary to identify and separate the contrast resulting from unintended propagation effects from the ones truly correlated to a varying optoelectronic response. One illustrative example of this phenomenon originates from the excitation of propagating surface polaritons, which can be mediated by the nearby metallic probe tip. This exciting idea has proven valuable in the study of the properties of such surface waves [19,28]. However, recent studies have shown that more subtle and confounding effects can also occur. In some cases, subwavelength structures can exhibit near-field contrast that is unrelated to any spatially varying conductivity or surface wave, but rather to their electrostatic interactions with distant (compared to the tip size) elements. For example, electrically grounded and electrically isolated metallic pads, otherwise identical, produce markedly different responses. Indeed, metallic disks of different sizes also produce different responses, even though they are all large in comparison to the tip apex. A simple electrostatic model can capture the essence of this behavior [34], although obviously, a more accurate treatment will require a more sophisticated analysis.

In this letter, we demonstrate that the shape, size, and orientation of a metallic pattern can have a profound influence on the measured near-field signal, even if the variation in structural properties takes place outside of the illuminated near-field region. In other words, the variations in image contrast described below cannot be described in the context of a purely electrostatic model, but must include propagation effects. Indeed, previous works have shown that surface or bulk plasmons may arise in metal or semiconductor nanostructures when illuminated in the near-field with single-frequency infrared radiation [35,36]. We, on the other hand, demonstrate a distinct effect mediated by the intrinsic electromagnetic excitations of the metallization itself, and employ *broadband* THz pulses coupled to our nanoscale AFM tip; THz enhancement, confinement, and propagation characteristics of metal nanostructures are actively under investigation [37], and our results highlight some of the mechanisms by which unique THz propagation effects can occur and be measured on the nanoscale. Moreover, future studies may be done to observe similar effects in s-SNOM image contrast at other wavelengths, not just in the THz regime.

2. Results and discussion

We use an atomic force microscope (AFM) (Neaspec GmbH, Germany) and PtIr-coated probe tips (Rocky Mountain Nanotechnology, USA) with 40 nm tip radius and 80 μm shank length to perform near-field THz time-domain spectroscopy (THz-TDS) [38–42]. Broadband (0.2-2 THz) single-cycle pulses are generated using a GaAs photoconductive antenna (TeraSed, Laser Quantum), focused onto the AFM tip, elastically scattered in a near-forward direction from the tip-sample system, and detected outside of the AFM using free-space electro-optic sampling with a lock-in amplifier referenced to a harmonic of the tip-tapping frequency (~24 kHz). The scattered THz pulses are detected coherently in the time domain, allowing us to obtain a material's full THz spectral response via Fourier transform. We can either measure a time-domain waveforms at a fixed sample position or detect the peak scattered signal (at a fixed time delay) and raster-scan over the structure to generate THz near-field images. Topographical and optical near-field data are obtained simultaneously in our AFM.

As shown in Fig. 1(a), our sample is comprised of a gold pattern, lithographically deposited on a SiO_2 substrate, with 70 nm thickness. The pattern consists of 11 gold disks, each 2.5 μm in diameter, each connected to a large gold ground pad by 700 nm wide, 70 nm thick metal lines of different lengths, ranging from approximately 5 μm to 115 μm. We scan the tip across each gold disk to generate a series of 11 6×1-μm images which capture the peak of the scattered THz signal both on top of the disk and on the nearby surrounding glass substrate. These 11 images are shown in Fig. 2(a), in order from shortest to longest ground line.

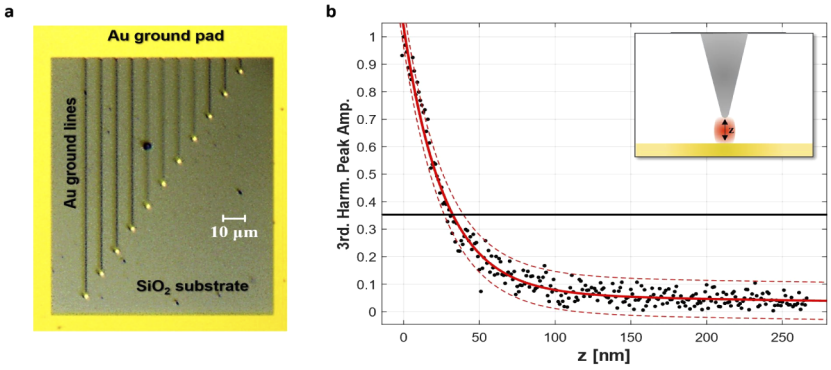

Fig. 1. (a) Photo of the Au and SiO_2 structure, taken using the AFM's top-down camera. 11 identical disks are connected to a large gold pad by conducting ground lines of lengths approximately 5, 16, 27, 40, 52, 63, 75, 85, 95, 106, and 115 μm. Dimensions of the disk are determined by AFM topography imaging while lengths of the ground lines are determined using the AFM camera's built- in scale bar (50 μm bar shown for scale). (b) 3rd harmonic approach curve (schematic shown in inset) on the ground pad region, with data denoted by black dots and double-exponential fit as the solid red line. Dashed lines mark 95% confidence in fit interval. 1/e line shown in solid black.

For this work, we perform most of our analysis with images and time-domain waveforms demodulated at the 3rd harmonic of the tip tapping frequency; it is generally accepted that 2nd or 3rd harmonic demodulation is acceptable for sufficient far-field background suppression [43] to achieve approximately tip-size-limited spatial resolution. The exact quantitative relationship between the tip size, field confinement, and imaging resolution is complicated and is still an active area of study [44–46]. Obtaining an accurate measure of the spatial resolution by scanning over a gold-to-SiO_2 boundary is challenging due to edge-darkening and other AFM imaging artifacts, as well as the imperfect edge profile of the lithographically-deposited gold. Instead, we acquire an approach curve [Fig. 1(b)] in which we measure the peak of the scattered THz signal on a bulk gold region as the tip-sample distance is gradually increased. The peak signal vs. z is fit to a double exponential function, with one term representing the quickly-decaying near-field signal, and the other representing a much more slowly decaying background, whose contribution becomes very small at higher ($n \geq 2$) harmonics. We then estimate the field confinement, and thus the lateral spatial resolution, by the 1/e width of these fits [41,42]. With this technique, we estimate a maximum THz imaging resolution of 31 5 nm at the 3rd harmonic, where the uncertainty is calculated from 95% error bounds of the exponential fit. We note that this estimate is below the 40 nm radius size of our tip; this may be due to small errors in tip fabrication, a chipped/damaged tip which could result in an artificially sharper-than-intended apex, or simply the extremely complex interplay between tip radius, length, shape, and resolution. Regardless, this value is consistent with a resolution that is tip-size-limited, with a confinement on the order of $\lambda/10^4$, and we therefore confirm our measurements are indeed probing the near field regime. We also note that this spatial resolution is roughly 80 times smaller than the diameter of the gold disks whose images are shown in Fig. 2.

The data shown in Fig. 2(a) contain evidence of the importance of the length of the grounding line connecting these disks to the nearby ground pad. We note that there is some variation in the on-disk signal which is dependent on the length of its associated ground line, and we attribute this to scattering properties of the gold ground pad Supplement 1, section 1). The images of the disks with the longest and shortest ground lines are otherwise unexceptional; a large contrast is visible between the gold disk structures and the SiO_2 backing, unsurprisingly suggesting a

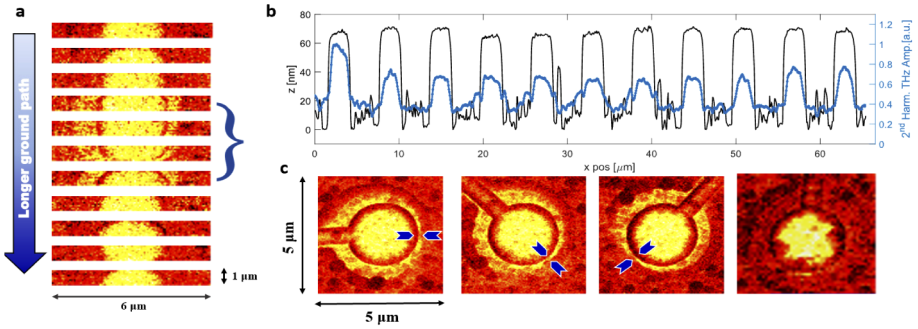

Fig. 2. (a) 6 µm × 1 µm scans across each of the 11 disks seen in Fig. 1(a). The red regions indicate less scattered signal (lower reflectivity) and yellow regions indicate more (higher reflectivity). The length of the metal ground line increases from top to bottom. "Halos" of high THz reflection in the regions outside of the metal disk are clearly visible around the 4^{th}-7^{th} of these images, corresponding to ground lines of 40-75 µm length. (b) 3^{rd} harmonic THz reflection line-scans across each disk (blue) stitched together along with corresponding topography (black); all disks are physically identical in both radius and height. The halos are visible outside of the raised disks, as enhanced signal strength outside of the region defined by the metallization. (c) THz images of disk #6, with 63 µm ground line length, measured in three different rotational orientations relative to the angle of the incident beam. Unique mode shape identically changes orientation, suggesting that the halo is an electrodynamic phenomenon associated with a true near-field signal, and not an imaging artifact. At right is disk #1, which shows no halo effect at all. In these four images, the incident wave is entering from the upper right.

much higher conductivity in the metallic regions and therefore increased local THz reflection. Clear contrast is visible even up to 5^{th} harmonic demodulation (Supplement 1, section 2), further indicating excellent coupling of the THz radiation to the tip. However, the disks with mid-length ground lines–ranging from 40–75 µm–show a surprising feature: an approximately 1-µm-wide "halo" of increased THz reflection appears in the regions around these disks. Because all 11 disks are identical, with an identical bulk SiO_2 substrate, these halos must be unrelated to the materials' dielectric properties; rather, they appear to arise from some effect related to the configuration of the surrounding gold structure. Notably, as shown in Fig. 2(c), the "halo" around a given disk has a unique and repeatable shape, with its thinnest section (indicated by blue arrows) always located opposite the point where the ground line contacts the disk. When the disk is rotated relative to the incident beam, this shape rotates along with it. This result indicates that the halo phenomenon is indeed a near-field enhancement associated with the metal structure and not a mere artifact of some inherent asymmetry of the imaging process. We also observe that a clear "edge-darkening" effect is visible for all disks in Fig. 2; this is a widely known but little-understood imaging artifact [13,47], occurring when the tip scans along topography which changes rapidly over a short distance. However, we have no reason to suspect this effect is significant or related to the halo noted above; Fig. 2(b) shows averaged line scans from Fig. 2(a) of the peak THz signal (blue) along with the averaged topography (black); the topographical scans confirm that all the disks are physically identical in smoothness, height, and width. The fact that the halo is observed for some disks but not others indicates that it is not simply a topographical artifact.

One plausible explanation for this halo phenomenon is that it arises from an electromagnetic standing wave excited between the metal disk and the metal ground plane, supported by the metal ground line. In essence, this requires that the metal ground line be considered as a waveguide of length comparable to λ. It has been shown that single conducting wires can be effective for propagating long-wavelength radiation with low attenuation [48–50]. Due to gold's negative

dielectric constant at THz frequencies and its finite conductivity, THz waves may be constrained to the gold-SiO_2 or gold-air dielectric interfaces, forming a Goubau-Sommerfeld wave [51] and propagating along the structure [52]. We envision that these waves are generated near the disk, propagate down the ground line, are partially reflected at the impedance mismatch caused by the ground line-ground plane boundary, and propagate back. As in a standard waveguide, paths with certain lengths can generate standing waves for a given frequency, with constructive interference at the ends. This may cause a sustained and enhanced field in the region near the disk, where the waveguide structure terminates. These waves, similar to TEM modes in a traditional coaxial waveguide [53], will have some characteristic guided wavelength related in a complex way to the free-space excitation frequency. Because our experiment is broadband, we must consider the implications of this guided wave phenomenon across the entire frequency range spanned by the incident THz pulse, in order to evaluate the validity of this description.

To explore this question, we first perform frequency-domain finite-element (FD-FEM) simulations to examine the waveguide behavior of the metallic ground lines. We recreate the rectangular ground path structures in cross-section [Fig. 3(a), inset] and perform a mode analysis. We examine the vertical electric field behavior of the lowest-loss modes and calculate the wavelength of the guided wave along the structure when excited with THz radiation; this mode analysis assumes that the structure is infinitely long and invariant along its length. We confirm that the structure supports a single low-loss and long-wavelength mode, with significant field enhancement confined to the boundaries of the gold ground line [shown in cross section in Fig. 3(a)]. Of course, the ground paths are *not* infinite, but rather they terminate on one side with a ground plane and on the other with a disk; regardless, these simulations establish the existence of a single low-loss Goubau-Sommerfeld mode on these lines. Figure 3(b) shows the dependence of the guided mode's wavelength on the radiation frequency as well as the frequency spectrum obtained experimentally from the scattering of our THz pulses from a large flat gold surface. These wavelengths range from approximately 150 μm with 0.4 THz excitation to 75 μm with 2 THz excitation. Standing waves of one-half-wavelength would therefore occur on ground lines with lengths between about 38 and 75 μm, precisely the range in which we observe the anomalous halos in our THz images.

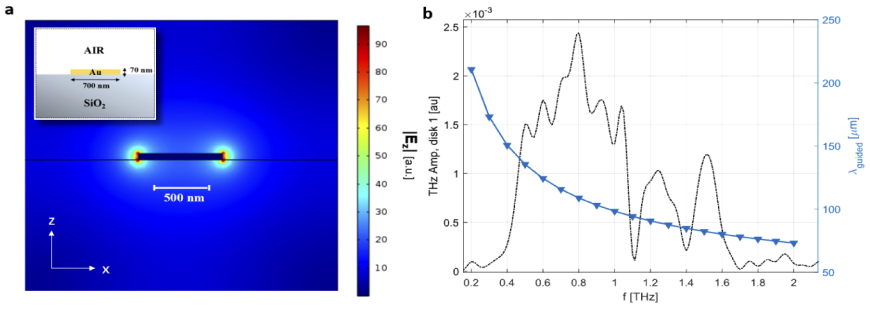

Fig. 3. COMSOL FD-FEM simulation of the ground path in cross-section. (a) Schematic of the structure (inset), and $|E_z|$ of the long- wavelength mode. Field is greatly enhanced at edges of gold structure, suggesting the ground path acts as a transmission line for the THz radiation.

This Goubau-Sommerfeld wave toy model is effective for understanding the general behavior of an individual ground line. However, to establish the origin of the halo, we perform additional numerical simulations to include the frequency dependence of the incident THz pulse, as well as the possible interplay between the components of the gold structure. To do this, we recreate the entire structure in 3 dimensions in a new FD-FEM model and compute its broadband near-field THz scattering properties. In these simulations, a THz wave is incident in the (–*x*, -*y*, -*z*)

direction, denoted by the white arrow in Fig. 4 (with an into-the-page component). We perform 19 simulations, each at a unique single frequency, in order to determine the structure's response from 0.2 to 2 THz in increments of 0.1 THz. These 19 results are superposed, with each one weighted according to that frequency's relative strength in our input pulse's amplitude spectrum. The resulting prediction of the strength of the vertical component of the electric field on the surface of the SiO_2 substrate is shown in Fig. 4. We find good agreement between these results and our experiment; disks with intermediate length ground lines show a higher field enhancement in a small halo region around the exterior of the disk, whereas disks with the longest and shortest ground lines show no such effect. We also note that, on the longest ground lines, we see clear evidence of nodes and anti-nodes in the simulation, indicating that the mode excited on these lines forms a standing wave pattern between the excitation point (the disk) and the ground plane. This standing wave pattern is the origin of the enhanced near-field signal which manifests itself as a halo around some of the disks, depending on the length of the ground line and the spectrum of the incident radiation. These results are highly dependent on the precise material composition of the structure, and we indeed find that varying the substrate material produces a significant change in the location of the electromagnetic "halos" (Supplement 1, section 3).

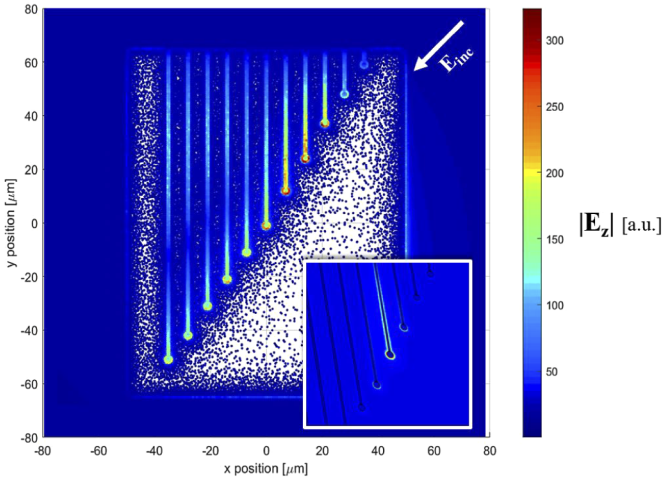

Fig. 4. FD-FEM simulation of the entire structure, shown from the top down. THz scattering is simulated at frequencies between 0.2 and 2 THz, in increments of 0.1 THz. The structure's response at each frequency is weighted by that frequency's strength in our spectrum (obtained experimentally) and added to obtain the total broadband scattering behavior. We confirm the appearance of an electromagnetic "halo" around disks of intermediate connector length. Inset shows zoomed-in simulation of halo appearing around disk with 52 μm long ground path, for 0.8 THz free space excitation.

We also observe some discrepancies between our measurements and simulations. Because the apex of our probe tip is very small (~40 nm) compared to the structure's disk size (~2.5 μm) and ground paths (~10s of μm), a full broadband numerical simulation that includes the metallic probe is computationally challenging. As such, this simulation result omits effects due to the tip and its electromagnetic interaction with the sample. For this reason, we do not expect perfect quantitative agreement between this simulation and the experimental results, and this is likely responsible for the fact that the simulation suggests the highest halo enhancement for disks with ground lines between 27-63 μm, whereas our experiment shows the strongest halos for disks with somewhat longer ground lines (between 40-75 μm). Indeed, we find that the inclusion of a conductive tip even at a single frequency changes the simulated THz scattering response

drastically, even in regions very far from the tip; measurements and additional simulations on another structure with 52 μm connectors and 8 disks of varying diameters suggest that the tip itself may enhance or completely eliminate these halos (see Supplement 1, section 4) Nevertheless, the substantial agreement between these simulations and our measurements strongly suggests that this standing wave model captures the essence of the physics.

3. Conclusion

In summary, we present THz near-field measurements of deeply subwavelength gold structures on a dielectric substrate and observe image contrast which does not correlate to changes in the local dielectric or topographic properties. The electromagnetic "halos" observed around the disks can be understood as a standing wave pattern formed by a Sommerfeld wave propagating along the ground lines connecting the disks to a large ground plane. The lengths of these grounding lines, which are a significant fraction of the free-space wavelength and much larger than the image resolution defined by the AFM tip size, define the frequency-dependent near-field response. This demonstrates that the particular shape, size, and orientation of wavelength-scale structures, even well outside the imaging region, can play a crucial role in determining the measured near-field response, often dwarfing the image contrast resulting from local conductivity changes.

In cases where the configuration of these structures is complicated, the measured local response cannot in general be easily predicted without performing a full simulation of the entire structure (which may, in many cases, be computationally challenging, as noted above). In the relatively simple case illustrated here (straight uniform metal lines connecting the image target to a ground plane), a simple standing wave model can provide a useful framework for understanding the results. However, in a more complex geometry, even this level of qualitative agreement may not be easy to obtain. We have observed that subwavelength metallic structures comparable to the one shown above yield markedly different results in simulation and experiment which *cannot* be explained with a simple waveguide model (see Supplement 1, section 4). As such, this technique may be used to probe electromagnetic excitations in metallic or waveguide-like structures on the nanoscale; however, in samples with anything but the simplest geometry, extra care must be taken when attempting to extract local dielectric properties from THz near-field spectroscopy.

Funding. National Science Foundation; Division of Materials Research; Division of Electrical, Communications and Cyber Systems; Solar System Exploration Research Virtual Institute (80NSSC19MO2015); Honeywell Federal Manufacturing and Technologies (DE-NA0002839); U.S. Department of Energy.

Acknowledgments. We also acknowledge valuable support and discussions with Dr. Joshua Trujillo of KCNSC. Authors from Stony Brook University also acknowledge support from the RISE2 node of NASA's Solar System Exploration Research Virtual Institute under NASA Cooperative Agreement 80NSSC19MO2015.

Disclosures. The authors declare no conflicts of interest.

Data availability. The AFM optical images, FD-FEM simulations, and corresponding numerical data are available from the authors upon request.

Supplemental document. See Supplement 1 for supporting content.

References

1. X. Chen, D. Hu, R. Mescall, G. You, D. N. Basov, Q. Dai, and M. Liu, "Modern Scattering-Type Scanning Near-Field Optical Microscopy for Advanced Material Research," Adv. Mater. **31**(24), 1804774 (2019).
2. H. A. Bechtel, E. A. Muller, R. L. Olmon, M. C. Martin, and M. B. Raschke, "Ultrabroadband infrared nanospectroscopic imaging," Proc. Natl. Acad. Sci. **111**(20), 7191–7196 (2014).
3. J. M. Atkin, S. Berweger, A. C. Jones, and M. B. Raschke, "Nano-optical imaging and spectroscopy of order, phases, and domains in complex solids," Adv. Phys. **61**(6), 745–842 (2012).
4. S. Mastel, M. B. Lundeberg, P. Alonso-González, Y. Gao, K. Watanabe, T. Taniguchi, J. Hone, F. H. L. Koppens, A. Y. Nikitin, and R. Hillenbrand, "Terahertz Nanofocusing with Cantilevered Terahertz-Resonant Antenna Tips," Nano Lett. **17**(11), 6526–6533 (2017).
5. B. Knoll and F. Keilmann, "Enhanced dielectric contrast in scattering-type scanning near-field optical microscopy," Opt. Commun. **182**(4-6), 321–328 (2000).

6. B. Knoll, F. Keilmann, A. Kramer, and R. Guckenberger, "Contrast of microwave near-field microscopy," Appl. Phys. Lett. **70**(20), 2667–2669 (1997).
7. A. Imtiaz, T. M. Wallis, S.-H. Lim, H. Tanbakuchi, H.-P. Huber, A. Hornung, P. Hinterdorfer, J. Smoliner, F. Kienberger, and P. Kabos, "Frequency-selective contrast on variably doped p-type silicon with a scanning microwave microscope," J. Appl. Phys. **111**(9), 093727 (2012).
8. A. J. Huber, F. Keilmann, J. Wittborn, J. Aizpurua, and R. Hillenbrand, "Terahertz Near-Field Nanoscopy of Mobile Carriers in Single Semiconductor Nanodevices," Nano Lett. **8**(11), 3766–3770 (2008).
9. N. C. J. V. D. Valk and P. C. M. Planken, "Electro-optic detection of subwavelength terahertz spot sizes in the near field of a metal tip," Appl. Phys. Lett. **81**(9), 1558–1560 (2002).
10. H. Zhan, V. Astley, M. Hvasta, J. A. Deibel, D. M. Mittleman, and Y.-S. Lim, "The metal-insulator transition in VO2 studied using terahertz apertureless near-field microscopy," Appl. Phys. Lett. **91**(16), 162110 (2007).
11. S. G. Amarie, T. Ganz, and F. Keilmann, "Mid-infrared near-field spectroscopy," Opt. Express **17**(24), 21794–21801 (2009).
12. S. Bensmann, F. Gaußmann, M. Lewin, J. Wüppen, S. Nyga, C. Janzen, B. Jungbluth, and T. Taubner, "Near-field imaging and spectroscopy of locally strained GaN using an IR broadband laser," Opt. Express **22**(19), 22369–22381 (2014).
13. T. Taubner, R. Hillenbrand, and F. Keilmann, "Performance of visible and mid-infrared scattering-type near-field optical microscopes," J. Microsc. **210**(3), 311–314 (2003).
14. I. Amenabar, S. Poly, W. Nuansing, E. H. Hubrich, A. A. Govyadinov, F. Huth, R. Krutokhvostov, L. Zhang, M. Knez, J. Heberle, A. M. Bittner, and R. Hillenbrand, "Structural analysis and mapping of individual protein complexes by infrared nanospectroscopy," Nat. Commun. **4**(1), 2890 (2013).
15. M. Brehm, T. Taubner, R. Hillenbrand, and F. Keilmann, "Infrared Spectroscopic Mapping of Single Nanoparticles and Viruses at Nanoscale Resolution," Nano Lett. **6**(7), 1307–1310 (2006).
16. S. Dai, Z. Fei, Q. Ma, A. S. Rodin, M. Wagner, A. S. McLeod, M. K. Liu, W. Gannett, W. Regan, K. Watanabe, T. Taniguchi, M. Thiemens, G. Dominguez, A. H. C. Neto, A. Zettl, F. Keilmann, P. Jarillo-Herrero, M. M. Fogler, and D. N. Basov, "Tunable Phonon Polaritons in Atomically Thin van der Waals Crystals of Boron Nitride," Science **343**(6175), 1125–1129 (2014).
17. M. M. Qazilbash, M. Brehm, B.-G. Chae, P.-C. Ho, G. O. Andreev, B.-J. Kim, S. J. Yun, A. V. Balatsky, M. B. Maple, F. Keilmann, H.-T. Kim, and D. N. Basov, "Mott Transition in VO2 Revealed by Infrared Spectroscopy and Nano-Imaging," Science **318**(5857), 1750–1753 (2007).
18. M. Liu, A. J. Sternbach, and D. N. Basov, "Nanoscale electrodynamics of strongly correlated quantum materials," Rep. Prog. Phys. **80**(1), 014501 (2017).
19. J. Chen, M. Badioli, P. Alonso-González, S. Thongrattanasiri, F. Huth, J. Osmond, M. Spasenović, A. Centeno, A. Pesquera, P. Godignon, A. Z. Elorza, N. Camara, F. J. G. de Abajo, R. Hillenbrand, and F. H. Koppens, "Optical nano-imaging of gate-tunable graphene plasmons," Nature **487**(7405), 77–81 (2012).
20. M. Filimon, I. Kopf, F. Ballout, D. A. Schmidt, E. Bründermann, J. Rühe, S. Santer, and M. Havenith, "Smart polymer surfaces: mapping chemical landscapes on the nanometre scale," Soft Matter **6**(16), 3764–3768 (2010).
21. E. A. Muller, B. Pollard, and M. B. Raschke, "Infrared Chemical Nano-Imaging: Accessing Structure, Coupling, and Dynamics on Molecular Length Scales," J. Phys. Chem. Lett. **6**(7), 1275–1284 (2015).
22. J. Lloyd-Hughes and T.-I. Jeon, "A Review of the Terahertz Conductivity of Bulk and Nano-Materials," J. Infrared, Millimeter, Terahertz Waves **33**(9), 871–925 (2012).
23. C. Liewald, S. Mastel, J. Hesler, A. J. Huber, R. Hillenbrand, and F. Keilmann, "All-electronic terahertz nanoscopy," Optica **5**(2), 159–163 (2018).
24. T. V. A. Nguyen, A. N. Hattori, M. Nagai, T. Nakamura, M. Ashida, and H. Tanaka, "Electrical transport properties of (La,Pr,Ca)MnO3 nanowires investigated using terahertz time domain spectroscopy," J. Appl. Phys. **119**(12), 125102 (2016).
25. Y. Gao, S. Kaushik, E. J. Philip, Z. Li, Y. Qin, Y. P. Liu, W. L. Zhang, Y. L. Su, X. Chen, H. Weng, D. E. Kharzeev, M. K. Liu, and J. Qi, "Chiral terahertz wave emission from the Weyl semimetal TaAs," Nat. Commun. **11**(1), 720 (2020).
26. B. C. Park, T.-H. Kim, K. I. Sim, B. Kang, J. W. Kim, B. Cho, K.-H. Jeong, M.-H. Cho, and J. H. Kim, "Terahertz single conductance quantum and topological phase transitions in topological insulator Bi2Se3 ultrathin films," Nat. Commun. **6**(1), 6552 (2015).
27. J. Zhang, X. Chen, S. Mills, T. Ciavatti, Z. Yao, R. Mescall, H. Hu, V. Semenenko, Z. Fei, H. Li, V. Perebeinos, H. Tao, Q. Dai, X. Du, and M. Liu, "Terahertz Nanoimaging of Graphene," ACS Photonics **5**(7), 2645–2651 (2018).
28. M. A. Huber, F. Mooshammer, M. Plankl, L. Viti, F. Sandner, L. Z. Kastner, T. Frank, J. Fabian, M. S. Vitiello, T. L. Cocker, and R. Huber, "Femtosecond photo-switching of interface polaritons in black phosphorus heterostructures," Nat. Nanotechnol. **12**(3), 207–211 (2017).
29. A. J. Huber, D. Kazantsev, F. Keilmann, J. Wittborn, and R. Hillenbrand, "Simultaneous IR Material Recognition and Conductivity Mapping by Nanoscale Near-Field Microscopy," Adv. Mater. **19**(17), 2209–2212 (2007).
30. H.-T. Chen, R. Kersting, and G. C. Cho, "Terahertz imaging with nanometer resolution," Appl. Phys. Lett. **83**(15), 3009–3011 (2003).
31. R. Hillenbrand and F. Keilmann, "Complex Optical Constants on a Subwavelength Scale," Phys. Rev. Lett. **85**(14), 3029–3032 (2000).

32. A. Cvitkovic, N. Ocelic, and R. Hillenbrand, "Analytical model for quantitative prediction of material contrasts in scattering-type near-field optical microscopy," Opt. Express **15**(14), 8550–8565 (2007).
33. A. A. Govyadinov, I. Amenabar, F. Huth, P. S. Carney, and R. Hillenbrand, "Quantitative Measurement of Local Infrared Absorption and Dielectric Function with Tip-Enhanced Near-Field Microscopy," J. Phys. Chem. Lett. **4**(9), 1526–1531 (2013).
34. X. Chen, X. Liu, X. Guo, S. Chen, H. Hu, E. Nikulina, X. Ye, Z. Yao, H. A. Bechtel, M. C. Martin, G. L. Carr, Q. Dai, S. Zhuang, Q. Hu, Y. Zhu, R. Hillenbrand, M. Liu, and G. You, "THz Near-Field Imaging of Extreme Subwavelength Metal Structures," ACS Photonics **7**(3), 687–694 (2020).
35. Y. Zhou, R. Chen, J. Wang, Y. Huang, M. Li, Y. Xing, J. Duan, J. Chen, J. D. Farrell, H. Q. Xu, and J. Chen, "Tunable Low Loss 1D Surface Plasmons in InAs Nanowires," Adv. Mater. **30**(35), 1802551 (2018).
36. M. M. Wiecha, S. Al-Daffaie, A. Bogdanov, M. D. Thomson, O. Yilmazoglu, F. Küppers, A. Soltani, and H. G. Roskos, "Direct Near-Field Observation of Surface Plasmon Polaritons on Silver Nanowires," ACS Omega **4**(26), 21962–21966 (2019).
37. Y.-M. Bahk, D. J. Park, and D.-S. Kim, "Terahertz field confinement and enhancement in various sub-wavelength structures," J. Appl. Phys. **126**(12), 120901 (2019).
38. H. G. von Ribbeck, M. Brehm, D. W. van der Weide, S. Winnerl, O. Drachenko, M. Helm, and F. Keilmann, "Spectroscopic THz near-field microscope," Opt. Express **16**(5), 3430–3438 (2008).
39. N. A. Aghamiri, F. Huth, A. J. Huber, A. Fali, R. Hillenbrand, and Y. Abate, "Hyperspectral time-domain terahertz nano-imaging," Opt. Express **27**(17), 24231–24242 (2019).
40. K. Moon, H. Park, J. Kim, Y. Do, S. Lee, G. Lee, H. Kang, and H. Han, "Subsurface nanoimaging by broadband terahertz pulse near-field microscopy," Nano Lett. **15**(1), 549–552 (2015).
41. A. Pizzuto, D. M. Mittleman, and P. Klarskov, "Laser THz emission nanoscopy and THz nanoscopy," Opt. Express **28**(13), 18778–18789 (2020).
42. P. Klarskov, H. Kim, V. L. Colvin, and D. M. Mittleman, "Nanoscale Laser Terahertz Emission Microscopy," ACS Photonics **4**(11), 2676–2680 (2017).
43. L. Wang and X. G. Xu, "Scattering-type scanning near-field optical microscopy with reconstruction of vertical interaction," Nat. Commun. **6**(1), 8973 (2015).
44. C. Maissen, S. Chen, E. Nikulina, A. Govyadinov, and R. Hillenbrand, "Probes for Ultrasensitive THz Nanoscopy," ACS Photonics **6**(5), 1279–1288 (2019).
45. K.-T. Lin, S. Komiyama, and Y. Kajihara, "Tip size dependence of passive near-field microscopy," Opt. Lett. **41**(3), 484–487 (2016).
46. S. Mastel, A. A. Govyadinov, C. Maissen, A. Chuvilin, A. Berger, and R. Hillenbrand, "Understanding the Image Contrast of Material Boundaries in IR Nanoscopy Reaching 5 nm Spatial Resolution," ACS Photonics **5**(8), 3372–3378 (2018).
47. A. Bek, R. Vogelgesang, and K. Kern, "Apertureless scanning near field optical microscope with sub-10 nm resolution," Rev. Sci. Instrum. **77**(4), 043703 (2006).
48. T. C. K. Rao and M. Hamid, "Mode spectrum of the modified Goubau line," Proc. Inst. Electr. Eng. **126**(12), 1227–1232 (1979).
49. K. Wang, A. Barkan, and D. M. Mittleman, "Propagation effects in apertureless near-field optical antennas," Appl. Phys. Lett. **84**(2), 305–307 (2004).
50. A. Sommerfeld, Electrodynamics (Academic Press, New York, 1952), Vol. 3.
51. A. Treizebre, T. Akalin, and B. Bocquet, "Planar excitation of Goubau Transmission Lines for THz BioMEMS," IEEE Microw. Wirel. Compon. Lett. **15**(12), 886–888 (2005).
52. T.-I. Jeon, J. Zhang, and D. Grischkowsky, "THz Sommerfeld wave propagation on a single metal wire," Appl. Phys. Lett. **86**(16), 161904 (2005).
53. K. Wang and D. M. Mittleman, "Metal wires for terahertz wave guiding," Nature **432**(7015), 376–379 (2004).